Retrievals of dust-related particle mass and ice-nucleating particle concentration profiles with ground-based polarization lidar and sun photometer over a central China megacity

Yun He[1,2,3], Yunfei Zhang[1,2,3], Fuchao Liu[1,2,3], Zhenping Yin[1,2,3], Yang Yi[1,2,3], Yifan Zhan[1,2,3], Fan Yi[1,2,3]

[1] School of Electronic Information, Wuhan University, Wuhan 430072, China.
[2] Key Laboratory of Geospace Environment and Geodesy, Ministry of Education, Wuhan 430072, China.
[3] State Observatory for Atmospheric Remote Sensing, Wuhan 430072, China.

Correspondence to: Yun He (heyun@whu.edu.cn)

Abstract. The POLIPHON (Polarization Lidar Photometer Networking) method is a powerful pathway to retrieve the height profiles of dust-related particle mass and ice-nucleating particles (INP) concentrations. The conversion factors fitted from the sun photometer observation data are the major part of the POLIPHON computations, which can convert the polarization-lidar-derived dust extinction coefficients into the dust-related particle mass and INP concentrations. For a central China megacity Wuhan (30.5°N, 114.4°E), located at the downstream area several thousands of kilometers far away from the source regions of Asian dust, dust particles always mix with other aerosols from local emission. Therefore, very few dust case data sets can be available when using the column-integrated Ångström exponent (for 440-870 nm) <0.3 and aerosol optical depth (at 532 nm) >0.1 recorded by sun photometer as the filtering criteria. Instead, we present another dust-case data-set screening scheme that applies the simultaneous polarization lidar observation to verify the occurrence of dust. Based on the 33 dust-intrusion days identified during 2011-2013, the extinction-to-volume ($c_{v,d}$) and extinction-to-large particle (with radius >250 nm) number concentration ($c_{250,d}$) conversion factors are determined to be $(0.52 \pm 0.12) \times 10^{-12}$ Mm m³m⁻³ and 0.19 ± 0.05 Mm cm⁻³, respectively. The $c_{250,d}$ for Wuhan is 27% larger than that observed at Lanzhou SACOL (36.0°N, 104.1°E), a site closer to the Gobi Desert, and trends to be closer to those observed in North Africa and Middle East, indicating dust aerosols from these two sources are also possibly involved in the dust events observed over Wuhan. As a comparison, the conversion factor $c_{290,c}$ of 0.11 ± 0.02 Mm cm⁻³ for continental aerosol is much smaller than $c_{250,d}$, indicating that there is no significant influence of urban aerosols on the retrievals of dust-related conversion factor over Wuhan. The conversion factors are applied in a dust event in Wuhan to reveal the typical dust-related immersion-mode INP concentration over East Asia city. The proposed dust-case data-set screening scheme may potentially be extended to the other polluted city sites more influenced by mixed dust.

1 Introduction

Aerosol-cloud interactions, also named 'aerosol indirect effects', significantly impact the global climate (Rosenfeld et al., 2014). The interactions show an overall cooling effect on radiative forcing, while with the largest uncertainty, meaning that they are still poorly understood and thus, not well represented in the climate model (IPCC, 2013). Heterogeneous nucleation is one of the most important aerosol-cloud interactions for mixed-phased clouds, which are essential to cloud electrification and the production of precipitation (Rosenfeld et al., 2008; Mülmenstädt et al. 2015). At temperatures ranging from -38°C to 0°C, ice crystals within the mixed-phase cloud are primarily produced via heterogeneous freezing with some types of insoluble aerosols acting as ice-nucleating particles (INPs) (Cantrell and Heymsfield, 2005).

Numerous types of aerosols can be served as INP as reviewed by Murray et al. (2012) and Kanji et al. (2017), including mineral dust, biological material, volcanic ash, etc. Dust is the dominant type accounting for 77% of active INPs ubiquitous all over the world and thus, provides a great opportunity to study heterogeneous nucleation (Hoose et al. 2010). In principle, one INP can correspondingly form one ice crystal particle except for the occurrence of ice multiplication mechanism (also named Hallett-Mossop process) at temperatures of -3 to -8°C (Hallett and Mossop, 1974), which can rapidly enhance the number concentration of the ice population following initial primary ice nucleation events (Field et al., 2017). This agreement was substantially verified by a closure study on dust-related altocumulus and cirrus layers, which compared the lidar-derived ice-nucleating particle concentration (INPC) with the radar-derived ice crystal number concentration (ICNC) and found that the discrepancy between them was within one order of magnitude (Ansmann et al., 2019a). Moreover, good agreement between INPC derived by the measurements of CALIPSO spaceborne lidar and ICNC derived by the synergistic measurements of spaceborne raDAR and liDAR (DARDAR) was also found by Marinou et al. (2019). Therefore, it is of significant importance to quantitatively estimate INPC profiles, which provides an approach to evaluate the ICNC parameterization that may be necessary for climate models.

The POLIPHON (Polarization Lidar Photometer Networking) method, first introduced by Ansmann et al. (2012), is able to retrieve the height profiles of dust-related INPC and dust mass concentration. In this approach, two remote sensing instruments, lidar and sun photometer, together with an INP parameterization scheme are employed (Mamouri and Ansmann, 2014, 2015, 2016; Mamali et al., 2018; Ansmann et al., 2019a, 2019b, 2020; Hofer et al., 2020). Marinou et al. (2019) compared the INPC profiles retrieved by lidar observation with those measured by unmanned aerial vehicles (UAVs). A good coincidence within one order of magnitude was found applying the parameterization scheme U17-D from Ullrich et al. (2017), meaning that the POLIPHON method is a promising approach to retrieve the INPC height profiles. Furthermore, the cost of such a remote sensing approach is much less than the airborne in situ observation, making it applicable for long-term INPC monitoring both locally and globally.

To retrieve the dust-related INPC profiles, the most significant aspect is the estimation of dust-related conversion factors that can convert the dust extinction coefficient to large particle (with radius >250 nm) number concentration and dust mass concentration. For the regions in or near deserts, pure or quasi-pure dust cases frequently occur with less influence from other

aerosol emissions. Ansmann et al. (2019b) obtained the dust conversion factors for those Aerosol Robotic Network (AERO-NET) sites in or near the desert regions with the filtering criteria of an Ångström exponent (AE) for the 440-870 nm wavelength range AE <0.3 and a 532 nm (converted from 500 nm) aerosol optical depth (AOD) >0.1. The pure-dust-case data sets following the criteria given above can be found in quantity as shown by Ansmann et al. (2019b) (with adequate data points >2500 for each site). However, very few such data sets are available as seen in sun photometer observation for those cities located at the downstream regions of Asian dust, if such filtering criteria are applied. For example, the local aerosol emissions are always abundant during the dust-intrusion days in a central China megacity, e.g., Wuhan (30.5°N, 114.4°E) (see Figure 1) (Kong and Yi, 2015; Ma et al., 2019; Yin et al., 2021b). Therefore, the sun photometer-measured column-integrated aerosol properties are the result of a mixture of dust particles and other aerosols (i.e. mixed dust, usually with a lidar-measured particle depolarization ratio <0.3). Urban air pollution generally cannot affect the atmospheric INPC (Chen et al., 2018). Similarly, Kanji et al. (2020) and Schill et al. (2020) found that soot also is not an effective aerosol type serving as INP. However, their optical properties may have an impact on the retrievals of the dust-related conversion factors, and then the INPC for mixed dust situations in a megacity influenced by long-range transported dust plumes (Córdoba-Jabonero et al., 2018; Mamouri and Ansmann, 2017; Wang et al., 2021). To retrieve the dust-related POLIPHON conversion factors for Wuhan, we present another dust-case-selection scheme by means of simultaneous ground-based polarization observations, which can verify the dust occurrence. Using this method, the height profiles of INPC and dust mass concentration can be successfully obtained at Wuhan.

The organization of this paper is as follows. We first briefly introduce the relevant instruments and data. The following section shows the primary steps of the POLIPHON method as well as the retrieval scheme of two dust-related conversion factors for Wuhan. In Sect. 4, we present a case study on the dust-related heterogeneous nucleation process at Wuhan using the method given in Sect. 3. In the last section, conclusions and discussions are presented.

2 Instrumentation and Meteorological Data

2.1 Polarization Lidar

A zenith-pointed ground-based polarization lidar, installed at an atmospheric observatory on the campus of Wuhan University located at Wuhan, China (30.5°N, 114.4°E, ~80 m above sea level, the exact location can be seen in Figure 1), was employed to observe the transported dust (He et al, 2015) as well as the ice formation within the mixed-phase cloud routinely (He et al, 2021a, 2021b; Yin et al., 2021a). The lidar system has been described in detail by Zhang et al. (2014) and Kong and Yi (2015) and enables us to obtain the height profiles of the aerosol extinction coefficient (if assuming a typical local lidar ratio), aerosol backscatter coefficient, and volume/particle linear depolarization ratio at 532 nm. It should be mentioned that double cascaded cubic polarizing beamsplitters were used respectively for the parallel (P) and perpendicular (S) polarized channels so that the crosstalk between them can be well suppressed.

The temporal and height resolutions of lidar raw data are 1 minute and 3.75 m, respectively. The gain ratio between two orthogonally polarized channels is calibrated using the Δ90° method (Freudenthaler et al., 2009); the relative error for volume depolarization ratio δ (aerosol + molecular) is less than 5%. The lidar-derived δ is sensitive to the nonsphericity of backscattering targets, therefore can be employed in distinguishing dust aerosols from other types of spherical aerosols (He and Yi, 2015; Sakai et al., 2010). The method from Fernald (1984) was used to retrieve the aerosol backscattering coefficient β and backscatter ratio R; the uncertainties are estimated to be ≤10% for β and R. Then, the particle linear depolarization ratio δ_p at height z can be calculated by using the equation below:

$$\delta_p(z) = \frac{\delta(z)[R(z) + R(z)\delta_m - \delta_m] - \delta_m}{R(z) - 1 + R(z)\delta_m - \delta(z)}, \tag{1}$$

where δ_m (=0.004 for our lidar system) is the molecular depolarization ratio that is related to the specification of the narrowband filters in the receiving unit of the lidar system (Behrendt and Nakamura, 2002). The relative uncertainty for δ_p is generally on the order of 5-10 % (Mamouri et al., 2013).

2.2 Sun Photometer and GRASP Algorithm

A sun-sky scanning spectral photometer (CE-318) was installed at our observatory in April 2008 and had been operating until August 2013 (Zhang et al., 2021). It detects the direct solar irradiance at eight wavelengths (340, 380, 440, 500, 675, 870, 1020, and 1246 nm) for every 15 minutes; the AOD at each wavelength can then be calculated following the Beer-Lambert law. The uncertainties of AOD are ~0.015 at 440-1020 nm and ~0.035 at 340-380 nm under the optical air mass of 1.0 (Zhang et al., 2021), which is corresponding to the summer solstice in the Northern Hemisphere. Considering transported dust plumes generally intrude into Wuhan in spring and winter, these AOD uncertainties should be divided by a factor of 1.6 and 2.4, respectively. Therefore, the AOD uncertainties for our sun photometer should be nearly similar as those (0.01-0.02) for AERONET field instruments (Holben et al., 1998). The sky radiance data are not available. The fine mode fraction (FMF) of 500 nm AOD was obtained based on the method given by O'Neill et al. (2003). The uncertainty in FMF mainly depends on the assumptions of the coarse-mode Ångström exponent, spectral derivative coarse-mode Ångström exponent, and relationship between the fine-mode Ångström exponent and spectral derivative fine-mode Ångström exponent (O'Neill et al., 2001), which are related to the actual atmospheric condition.

Generalized Retrieval of Aerosol and Surface Properties (GRASP) algorithm is widely used in retrieving aerosol microphysical properties (Dubovik et al., 2014) and was reported to be applied in dust event observation (Benavent-Oltra et al., 2017, 2019). Although our sun photometer lacks the sky radiance observation, the GRASP-AOD application allows us to determine particle size distributions using only spectral AOD data (Torres et al., 2017). In this study, the column-integrated particle size distribution was retrieved using the spectral AODs ranging from 380 to 1020 nm as the input in the GRASP algorithm. Considering Wuhan is a megacity with plenty of local aerosol emissions (Ma et al., 2019), we assumed the complex refractive index values to reflect the mixed desert-dust characteristic in the particle size distribution inversion. The real part

was set to be 1.55; the imaginary part was set to be wavelength-dependent (i.e. 0.003 at 380 nm, 0.0025 at 440 nm, 0.0022 at 500 nm, 0.0014 at 675 nm, 0.001 at 870 nm, and 0.001 at 1020 nm) (Dubovik et al., 2002). When calculating the particle size distributions for continental aerosols (AE >1.6), the complex refractive index was set to be $1.47+0.014i$.

2.3 Radiosonde Data

The radiosondes (GTS1-2, made by China) were launched twice per day at 0800 Local Time (LT) (0000 UTC) and 2000 LT (1200 UTC) from the Wuhan Weather Station, located approximately 24 km from our lidar site. The profiles of temperature and pressure provided by radiosondes were used in the INP concentration parameterization (DeMott et al., 2010, 2015) to convert the aerosol particle (with radius >250 nm) number concentrations (APC_{250}) into the INP concentrations. The error for the measured temperature is less than 1 °C (Nash et al., 2011).

2.4 CALIOP

The Cloud-Aerosol Lidar and Infrared Pathfinder Satellite Observation (CALIPSO) satellite was launched in 2006 and carries an instrument Cloud-Aerosol Lidar with Orthogonal Polarization (CALIOP) to provide the vertical information of aerosols and clouds (Winker et al., 2007). The satellite orbit nearly passes Wuhan every day at about 0200 LT and 1400 LT with the nearest subpoint occurred per 16 days. Due to the change of its orbit height from 705 km to 688 km to resume formation flying with CloudSat, the closest horizontal distance between CALIPSO subpoint and our lidar site is <10 km before 13 September 2018 and <50 km currently. It can measure the elastic backscatter at both 532 nm and 1064 nm and is also capable of measuring the depolarization ratio at 532 nm near nadir during both daytime and nighttime. The depolarization ratio is used to identify the dust aerosol and the ice-containing cloud because of their nonspherical shape. The color ratio, defined as the ratio of backscattering at 1064 nm to backscattering at 532 nm, is provided as a measure of the particle size. In this study, the CALIOP Level-2 vertical feature mask (VFM) product was used not only to validate the presence of dust layers over Wuhan (Omar et al., 2009) but also to provide the three-dimension structure information on the dust plume combining simultaneous ground-based measurements (i.e., vertical distribution and horizontal extension).

2.5 HYSPLIT Model

The Hybrid Single Particle Lagrangian Integrated Trajectory (HYSPLIT) model, based on the National Centers for Environmental Prediction (NCEP) GDAS data product, can calculate the backward trajectory of the air mass (Draxler and Rolph, 2003). In this study, three-day backward simulations were regarded to check the potential source of the dust aerosol layers observed by polarization lidar over Wuhan.

3 Methodology

In this section, we introduce the retrieval schemes for dust-related particle mass and INP concentrations. The specific steps of the data processing were presented in previous literature (Mamouri and Ansmann, 2014, 2015, 2016). Here, we just present the main derivation steps (Sect. 3.1). More importantly, the retrieval scheme of dust-related conversion factors over Wuhan, a megacity that is thousands of kilometers far from desert regions, is shown in detail (Sect. 3.2). The methodological diagram is given in Fig. 2. The related data or algorithms applied for each step are showed. In particular, it should be emphasized that GRASP algorithm is only used in the step of deriving the particle size distribution from spectral AODs.

3.1 Retrieval scheme of dust mass concentration and dust-related INPC

First, aerosol backscatter coefficient β can be determined from the Mie backscatter lidar data with the Fernald Method (Fernald, 1984). Then, we need to separate dust component (i.e. β_d) from the total aerosol backscatter coefficient β using the so-called 'one-step' approach (Mamouri and Ansmann et al., 2014). The dust backscatter coefficient β_d can be converted into the dust extinction coefficient α_d by multiplying with a typical dust lidar ratio S_d. Finally, α_d can be related to the dust mass concentration and dust-related INPC with the conversion factors obtained by sun photometer data and according parameterizations (INPC).

The primary principle is introducing two threshold values of particle depolarization ratio, non-dust particle depolarization ratio $\delta_{nd} = 0.05$ and dust particle depolarization ratio $\delta_d = 0.31$ (Sakai et al., 2010), to separate the respective contribution of each component (dust particle, non-dust particle, and their mixture) to the total backscatter coefficient. The particles with $\delta_p < \delta_{nd}$ are considered as non-dust particles. The particles with $\delta_p > \delta_d$ are considered as pure dust particles (i.e. mineral dust). δ_p values range between δ_{nd} and δ_d are the mix of non-dust and pure dust components. The dust backscatter coefficient β_d can be expressed as (Tesche et al., 2009)

$$\beta_d(z) = \beta_p(z) \frac{(\delta_p(z) - \delta_{nd})(1 + \delta_d)}{(\delta_d - \delta_{nd})(1 + \delta_p(z))}, \tag{2}$$

The subscripts 'n', 'nd', and 'p' represent 'dust', 'non-dust', and 'particle' (dust + non-dust), respectively. Therefore, the dust extinction coefficient α_d can be calculated by:

$$\alpha_d(z) = \beta_d(z) \times S_d, \tag{3}$$

where the dust lidar ratio S_d is set to be 45 sr (Hu et al., 2020). The uncertainty in α_d mainly depends on the contribution of dust component within an aerosol layer. Very low dust contribution can cause a very large uncertainty in α_d (Marinou et al., 2019). Since δ_p values are mostly observed to be 0.14-0.43 over Wuhan during the dust-related heterogeneous nucleation events (He et al., 2021a), we only consider the well-detected desert dust layer ($\delta_p \approx 0.3$) and less pronounced aerosol layer ($\delta_p \approx 0.2$) when estimating the uncertainty in α_d. Mamouri and Ansmann (2014) estimated the uncertainty in β_d to be 15-20% for well-detected desert dust layers and 20-30% for less pronounced aerosol layers. Considering the uncertainty of ~10% in

updated dust lidar ratio (Peng et al., 2021), here the uncertainty in α_d is estimated to be 18-32%, which is more conservative than the values of 15-25% given by Ansmann et al. (2019b).

Finally, the dust mass concentration M_d can be computed by the equation below:

$$M_d(z) = \rho_d \times \alpha_d(z) \times c_{v,d}, \tag{4}$$

where ρ_d is the dust particle density (2.6 g cm^{-3} for Asian dust) (Wagner et al., 2009) and $c_{v,d}$ is the extinction-to-volume conversion factor. The value of $c_{v,d}$ can be obtained from sun-photometer-observed dust-intrusion days as discussed by Sect. 3.2. The uncertainty in M_d is estimated to be 29-64%.

To calculate the INPC, the dust extinction coefficient α_d need to be converted to the column-integrated number concentration of large particles with radius >250 nm APC_{250} (here denoted as $n_{250,d}$) by the expression:

$$n_{250,d}(z) = c_{250,d} \times \alpha_d(z), \tag{5}$$

where $c_{250,d}$ is the conversion factor obtained from sun photometer observation (see Sect. 3.2) during dust-intrusion days at our site. The overall uncertainty for $n_{250,d}$ is estimated to be 27-40%. Based on an INPC parameterization scheme given by DeMott et al. (2010, 2015) which is appropriate for dust-related immersion freezing regime, one can finally retrieve the height profile of INPC:

$$INPC(p_z, T_z) = [(T_0 p_z)/(T_z p_0)] \times INPC(p_0, T_0, T_z), \tag{6}$$

Here, INPC value under standard pressure ($p_0 = 1013$ hPa) and temperature ($T_0 = 273.16$ K) condition $INPC(p_0, T_0, T_z)$ can be expressed by the D10 parameterization scheme (DeMott et al. 2010):

$$INPC(p_0, T_0, T_z) = a \cdot (273.16 - T_z)^b \cdot n_{250,d}(p_0, T_0)^{[c(273.16-T_z)+d]}, \tag{7}$$

with the constants a = 0.0000594, b = 3.33, c = 0.0265, and d = 0.0033. This parameterization scheme is applicable for temperatures ranging from -9 °C to -35 °C. The D15 parameterization scheme is another option explicitly for mineral dust (DeMott et al. 2015):

$$INPC(p_0, T_0, T_z) = f_d \cdot n_{250,d}(p_0, T_0)^{[a_d(273.16-T_z)+b_d]} \cdot \exp[c_d(273.16 - T_z) + d_d], \tag{8}$$

with the constants $a_d = -0.074$, $b_d = 3.8$, $c_d = 0.414$, and $d_d = -9.671$. This parameterization scheme is applicable for temperatures ranging from -21°C to -35°C. The uncertainty for INPC using D15 is within an overall factor of 3 (Mamouri and Ansmann, 2015]. In practice, the corresponding meteorological parameter (i.e. pressure and temperature) profiles are provided by the measurement from the most recently launched radiosonde.

Note that these two parameterizations (D10 and D15) are used for immersion freezing. Ullrich et al. (2017) developed another important parameterization for heterogeneous ice nucleation that quantifies the INPC as a function of ice nucleation active surface site density (related to temperature and ice saturation ratio). This parameterization included both desert dust and soot aerosol and was applicable for both immersion nucleation and deposition nucleation. Most dust layers over Wuhan appear at relatively low altitudes with warmer meteorological conditions; hence, immersion nucleation takes place more generally. Therefore, we only applied D10 and D15 parameterizations in this study.

3.2 POLIPHON conversion factors over Wuhan

As mentioned in Sect. 3.1, we need to obtain the dust-related conversion factors. Ansmann et al. (2019b) reported an extended set of dust conversion factors considering all relevant deserts around the globe using the AERONET database. To obtain climatological dust conversion factors for a given AERONET site, they filtered all AERONET data sets with the criteria of an Ångström exponent for the 440-870 wavelength range AE <0.3 and a 532 nm (converted from 500 nm) AOD >0.1. The pure dust cases following the criteria given above can be found more easily (with adequate data sets >2500 for each site) in/near the desert regions, as presented in Ansmann et al. (2019b). Dust frequently intrudes into Wuhan. However, very few sun photometer data sets can fulfill those constraints. This is caused by plenty of local aerosol emissions (especially within the boundary layer), which make the column-integrated aerosol properties observed to generally reflect characteristics of mixed dust (dust particles mixed with other urban aerosols) (Shao et al., 2020; Liu et al., 2021; Yin et al., 2021b). It is also worthy to note that the previous gravitational sedimentation and wet deposition of dust particles during transport may modify the dust optical and microphysical properties above Wuhan. Thus, the dust-related conversion factors differ from those of near-desert sites.

To select the dust-containing data sets from sun photometer observations, for the first time, we employed the simultaneous ground-based polarization lidar observations as an auxiliary. Once a dust layer with δ >0.06 and layer thickness >0.9 km was observed by lidar (Huang et al., 2008), we considered the simultaneous observational data sets from sun photometer available for calculating the dust-related conversion factors. For a dust-intrusion day, all these dust-containing data sets measured by sun photometer were averaged to form a representative result (AOD and later calculated particle size distribution calculated by GRASP algorithm) of this day. Here, we give an example of the dust-case data-set screening scheme for a typical dust-intrusion day. Figure 3 presents the time-height contour plots of the range-corrected signal and volume depolarization ratio measured by polarization lidar during 1000-1600 LT on 28 April 2011. The lidar system began to operate at ~1000 LT this day. Two distinct dust layers with δ >0.1 can be identified from the surface to around 2.0 km and above 2.5 km, respectively. Hence, it was a typical dust-intrusion day. Besides, four cloud-free periods (1000-1030 LT, 1220-1250 LT, 1400-1430 LT, and 1530-1600 LT) were selected to show the vertical distributions of δ as seen in Fig. 4c, 4d, 4e, and 4f. The δ values were larger than 0.06 throughout the whole lower troposphere (from surface to around 5.5 km). Considering the thresholds of δ and thickness that we defined, all these periods can be identified as 'dust occurrence'.

The sun photometer observation results for the same day, including six-wavelength AODs, AE, FME, fine-mode and coarse-mode 500 nm AODs, are shown in Fig. 4. FMFs ranged from 0.2 to 0.3 during the dust intrusion period, indicating a significant contribution of large dust particles. Similar FMF values (0.2-0.4) were also reported at Ouarzazate (30.9°N, 6.9°W), Morocco during Saharan Mineral Dust Experiment 1 (SAMUM-1) (Ansmann et al., 2011; Mamouri and Ansmann, 2014). Nevertheless, AE values were 0.6-0.9, meaning that the mixed dust cases cannot fulfill the criteria for pure dust cases (AE < 0.3) as given by Ansmann et al. (2019b). As confirmed by the polarization lidar observation, the sun photometer data sets from a period of 1000-1550 LT were related to the dust intrusion. Therefore, the corresponding data sets measured by sun

photometer during this dust-intrusion period (1205-1550 LT) were averaged to form the representative results (AOD and later particle volume size distribution) for 28 April 2011. Figure 5 shows the column-integrated particle volume size distribution (Fig. 5a) and particle number size distribution (Fig. 5b) derived from the averaged spectral AODs during 1000-1550 LT on 28 April 2011 based on GRASP-AOD algorithm. The particle radius ranges from 0.05 to 15 μm and is separated into 43 radius intervals of logarithmically equal width.

The column APC_{250} values are obtained by integrating the particle number (as given in Fig. 5b) with radius larger than 250 nm. Considering dust is the dominated type in coarse-mode particles, we assume $APC_{250} = APC_{250,d}$, where the subscript 'd' denotes the dust component. Then, the relationship between $APC_{250,d}$ and 500 nm AOD can be linked by a conversion factor $c_{250,d}$ with the following equation:

$$c_{250,d} = \frac{APC_{250,d}}{AOD_{500}},$$
(9)

Assuming an aerosol layer thickness of D, we can convert the above equation to:

$$c_{250,d} = \frac{APC_{250,d}/D}{AOD_{500}/D} = \frac{n_{250,d}}{\alpha_d},$$
(10)

where $n_{250,d}$ and α_d are the layer-mean large particle (with radius >250 nm) number concentration and lidar-derived dust extinction coefficient, respectively. In total, we used 32 dust-intrusion days from joint lidar and sun photometer observations during 2011-2013. As seen in Fig. 6, a good correlation between $n_{250,d}$ and α_d was found with a linear Pearson correlation coefficient of 0.976 for the period of 2011-2013. Each green point represents a pair of daily averaged values for the dust-occurring period of a dust-intrusion day (taking the day of 28 April 2011 shown above as an example). Note that these points represent the same dataset (i.e., the same 33 dust-intrusion days) as those green points in Figure 5. The $c_{250,d}$ value was 0.19 ± 0.05 Mm cm^{-3} as computed by the equation below:

$$c_{250,d} = \frac{1}{J_d}\sum_{j=1}^{J_d} \frac{n_{250,d,j}}{\alpha_{d,j}},$$
(11)

The standard deviation of 0.05 Mm cm^{-3} is similar to those obtained from other AERONET sites (0.02-0.05 Mm cm^{-3}) by Ansmann et al. (2019b). The $c_{250,d}$ value of 0.19 Mm cm^{-3} is approximately 27% larger than the value of 0.15 Mm cm^{-3} obtained at Lanzhou SACOL (36.0°N, 104.1°E) AERONET site as well as at Dalanzadgad, Mongolia (see Fig. 1), which are very close to the source region of Asian dust (Ansmann et al., 2019b). Mamouri and Ansmann (2015) mentioned that this dust-related conversion factor can almost be invariable from dust source (Morocco and Cape Verde) to downwind regions (Barbados). Therefore, this discrepancy indicates that Wuhan may not be only influenced by Asian dust. Note that the conversion factor 0.19 Mm cm^{-3} is more like the values of 0.16-0.20 Mm cm^{-3} for the North Africa (Saharan dust) and Middle East, suggesting that dust aerosols from these two sources are also possibly involved in the dust events observed over Wuhan. This conjecture can be verified to some extent since the dust plumes over Wuhan can often be traced back to these two sources by HYSPLIT model simulation (He et al., 2021a). Kojima et al., (2006) confirmed that dust particles that have not undergone substantial aging or a cloud-processing event can be present thousands of kilometers from source regions. Furthermore, to analyze the potential impact of local emissions on $c_{250,d}$, the conversion factor for continental aerosols $c_{290,c}$

was also calculated for the period during 2008-2013 as seen from the purple points in Fig. 6 (Mamouri and Ansmann, 2016). The $c_{290,c}$ value of 0.11 ± 0.02 Mm cm^{-3} for Wuhan is similar to those of around 0.10 Mm cm^{-3} for the two city sites, Limassol, Cyprus (34.7°N, 33.0°E) and Leipzig, Germany (51.4°N, 12.4°E) (Mamouri and Ansmann, 2016), meaning that this value depicts a typical conversion factor for the urban aerosol situations. Similar to the results in Limassol and Leipzig (Fig. 7b in (Mamouri and Ansmann, 2016)), $c_{250,d}$ is almost twice larger than $c_{290,c}$ in Wuhan, indicating lesser large particles are included in the local pollutions. This comparison suggests that there is no significant influence of urban aerosols on the retrievals of dust-related conversion factor $c_{250,d}$ in Wuhan, at least for the 'most dusty' cases which we selected for $c_{250,d}$ calculation in this study.

The column particle volume concentration values V_d are obtained by integrating the entire particle size distribution spectrum. The relationship between V_d and 500 nm AOD can be linked by a so-called extinction-to-volume conversion factor $c_{v,d}$ with the following equation:

$$c_{v,d} = \frac{V_d}{AOD_{500}}, \tag{12}$$

Assuming an aerosol layer thickness of D, we can convert the above equation to:

$$c_{v,d} = \frac{V_d/D}{AOD_{500}/D} = \frac{v_d}{\alpha_d}, \tag{13}$$

where v_d and α_d are the layer-mean particle volume concentration and extinction coefficient, respectively. As seen in Fig. 7, a correlation between v_d and α_d was found with a linear Pearson correlation coefficient of 0.653 for the period of 2011-2013. Each point in Fig. 7 also represents a pair of daily averaged values for the dust-occurring period of a dust-intrusion day (taking the day 28 April 2011 shown above as an example). The $c_{v,d}$ value was $(0.52 \pm 0.12) \times 10^{-12}$ Mm m^{3}m^{-3} as computed by the equation below:

$$c_{v,d} = \frac{1}{J_d} \sum_{j=1}^{J_d} \frac{v_{d,j}}{\alpha_{d,j}}, \tag{14}$$

The conversion factor $c_{v,d}$ of 0.52×10^{-12} Mm m^{3}m^{-3} is approximately 32% smaller than the value of 0.77×10^{-12} Mm m^{3}m^{-3} obtained at Lanzhou SACOL AERONET site (Ansmann et al., 2019b), suggesting that the proportion of dust particles in the atmospheric column is relatively smaller in Wuhan. In particular, those more dispersed points below the dashed line seem to be more affected by anthropogenic aerosols. Moreover, the standard deviation of 0.12×10^{-12} Mm m^{3}m^{-3} for Wuhan locates in the varying interval of standard deviations $(0.05 - 0.17) \times 10^{-12}$ Mm m^{3}m^{-3} for the other AERONET sites in Ansmann et al. (2019b), meaning the $c_{v,d}$ value for Wuhan is justified.

Torres et al. (2017) analyzed the influence of AOD errors on the aerosol size distributions (in subsection 3.4 therein). The tests with random simulated errors showed that the uncertainties in the GRASP bimodal log-normal size distribution parameters increase as the aerosol loads decreases. Considering the averaging AOD_{440} (AOD at 440 nm) value of 0.92 for the 33 days selected in our study, we use the uncertainties in bimodal log-normal size distribution parameters from the coarse-mode aerosol prevailing case cluster with $AOD_{440} = 0.9$ (i.e., 'SOLV3' in Table 2 and 7 from Torres et al. (2017)) to estimate the uncertainty involved in APC_{250} and total volume concentration. The same AOD errors for each wavelength as AERONET

instruments were introduced. Taking the simulated uncertainties of GRASP bimodal log-normal size distribution parameters into account, the uncertainties in APC_{250} and total volume concentration caused by AOD errors are estimated to be <3.2% and ~0%. The uncertainty in AOD_{500} is ~2%. Torres and Fuertes (2021) compared the aerosol size properties derived by GRASP-AOD application with those obtained by AERONET retrieval algorithm. When AOD_{440} >0.4, the uncertainty in total volume concentration was estimated to be 23%. Mamouri and Ansmann (2015) mentioned that the uncertainty in AERONET algorithm derived APC_{250} is 10-15%. Propagating all the uncertainties above into the conversion factors obtained in this study, the derived uncertainties in $c_{250,d}$ and $c_{v,d}$ are conservatively estimated to be both <28%.

4 Case Study on a Dust-related Heterogeneous Nucleation Process

We used the two dust-related conversion factors $c_{250,d}$ and $c_{v,d}$ retrieved at Wuhan to analyze a dust-related heterogeneous nucleation case on 31 December 2017. Figure 8 presents the time-height contour plots (1 minute/30 m resolution) of the range-corrected signal (Fig. 8b) and volume depolarization ratio δ during 0100-0700 LT (Fig. 8d). The corresponding profiles of the relative humidity (RH), temperature (T), horizontal wind speed (V), and wind direction from the radiosonde launched at 0800 LT are shown in Fig. 8a and 8c. Two distinct dust aerosol layers (below ~2 km and at ~4.5-6.5 km, respectively) were identified with peak δ values exceeding 0.1. Another slight dust layer with an enhanced δ of ~0.04 occurred up to ~8 km after ~0230 LT.

According to the backward trajectories in Fig. 9, the dust layer below 2 km probably originated from the Taklimakan Desert. The two aloft dust layers were probably linked to the desert regions over northwest India and Pakistan. As seen from Fig. 10, the occurrence of dust over Wuhan was also verified by the vertical feature mask and aerosol subtype classification provided by the CALIOP Level-2 VFM data product. The satellite passed over Wuhan at ~1850 UTC on 30 December 2017 (0250 LT on 31 December 2017). The vertical dashed line denoted the location of the nearest subpoint to Wuhan. The two aerosol layers around Wuhan, respectively located at 0-2 km and ~4-5.5 km, were classified as the mix of dust (marked as '2', in yellow) and polluted dust (marked as '5', in brown).

As seen in Fig. 8d, an ice-containing cloud appeared at ~0405 LT at the altitudes where the upmost slight dust layer was located. The temperature at around 8 km was -32.5 °C as denoted by the horizontal dashed lines in Fig. 8. Therefore, the dust particles were likely to trigger the heterogeneous ice formation. Figure 11 shows the height profiles of optical properties including dust and total extinction coefficient, dust and total backscatter coefficient, volume depolarization ratio, and particle depolarization ratio during the period of 0320-0350 LT. The peak dust extinction coefficient for the upmost dust layer at an altitude of ~8.1 km was 2.0 Mm^{-1}. The peak particle depolarization ratio δ_p value for this slight dust layer was 0.16. The δ_p values of <0.3 were observed throughout the altitudes of 4-9 km, indicating the possible presence of mixed dust or fine-mode dust (Sakai et al., 2010).

In Fig. 12a, the dust extinction coefficients were converted into the dust mass concentrations by multiplying by the extinction-to-volume conversion factor $c_{v,d}$ and dust density. The maximum dust mass concentrations were 2.6 μg m^{-3} for the dust layer around 8 km and 46.0 μg m^{-3} for the dust layer at altitudes of 4.4-5.3 km. Note that more dense dust plumes could even be observed frequently in Wuhan. The dust mass concentrations of 6.27-154.79 μg m^{-3} had been observed in Wuhan for the dust events from December 2012 to December 2013 (He et al., 2021a). In Fig. 12b, the dust extinction coefficients were converted into the large particle number concentrations APC$_{250}$ by multiplying by the conversion factor $c_{250,d}$. Applying the INPC parameterization scheme D10 (DeMott et al., 2010) and D15 (DeMott et al., 2015), the immersion-mode ice-nucleating particle concentrations were finally retrieved as seen in Fig. 12c. The peak INPC value for the slight dust layer at an altitude of 8.1 km was 62.3 L^{-1} for D15 and 2,.7 L^{-1} for D10. The two parameterization schemes are in good agreement at temperatures ranging from -30 to -20 °C. These dust-related INPs might be related to the later-formed ice particles within the cloud at the same altitudes. It should be mentioned that, for deposition nucleation, another INPC parameterization scheme U17-D should be utilized (not shown herein) (Ullrich et al., 2017). Near the desert region, Jiang et al. (2016) found the INP concentrations can reach a level of several hundred per liter at -22 °C during a dust event in Xinjiang, northwest of China. For the downstream region of transported Asian dust, Chen et al. (2021) reported similar INP concentrations at -16 °C for 13 dust events in Beijing range from 0.42 to 17.36 L^{-1}. As more dense dust plumes were reported to appear frequently in Wuhan (He et al., 2021a), the INPC values much larger than 62.3 L^{-1} (D15) as observed in this case are probably present at other times, especially in the winter when the zero isotherms can drop to a lower height. This INPC level can have an important effect on ice nucleation in the atmosphere.

5 Discussions and Conclusions

The quantitative evaluation of dust-related INPC profiles is of particular interest for understanding the specific contribution of heterogeneous nucleation to the aerosol-cloud-interaction-induced radiative forcing. Furthermore, the understanding of INPC is also indispensable for estimating the impact of dust-related INPs on extreme precipitation (Zhang et al., 2020). However, when using the POLIPHON method to estimate the dust-related INPC profiles, the obtainment of dust-related conversion factors is not easy, but of great importance, for those cities over the downstream regions of long-range transported dust plumes. They may suffer the dual impact of the emissions of local pollution and transported dust aerosols. Urban air pollutions (e.g. anthropogenic PM$_{2.5}$ and black carbon) are generally considered not to affect the atmospheric INPC (Chen et al., 2018), thus the extraction of dust-related INP concentration using the powerful POLIPHON method is possible. In addition, the dust sedimentation and particle microphysical properties modification may also take place during the transport and thus, lead to the modified conversion factors over downstream cities compared with those over near-desert areas.

In this study, the retrievals of INPC and dust mass concentration mass profiles were realized for a central China megacity Wuhan (30.5°N, 114.4°E), located at the downstream region of long-range transported dust (see Fig. 1). Different from the previous screening scheme of dust occurrence data sets that simply employs the AOD at 532 nm >0.1 and Ångström expo-

nent for the 440-870 nm wavelength range <0.3 (Ansmann et al., 2019b) as the indicators of dust occurrence, ground-based polarization lidar observation was used as a useful auxiliary to verify whether dust particles were involved in a data set measured by sun photometer. In consequence, the dust-related conversion factors explicit for Wuhan (usually mixed dust) were obtained for the first time. The extinction-to-volume conversion factor $c_{v,d} = (0.52 \pm 0.12) \times 10^{-12}$ Mm m^{3}m^{-3} and the extinction-to-large particle (with radius >250 nm) number concentration conversion factor $c_{250,d} = 0.19 \pm 0.05$ Mm cm^{-3}. The $c_{250,d}$ for Wuhan is 27% larger than that observed at Lanzhou SACOL (36.0°N, 104.1°E) AERONET site that is much more closed to the source region of Asian dust, and is closer to those observed in North Africa and Middle East, meaning dust aerosols from these two sources are also possibly involved in the dust events observed over Wuhan. As a comparison, the conversion factor $c_{290,c}$ of 0.11 ± 0.02 Mm cm^{-3} for continental aerosol is much less than $c_{250,d}$, indicating that there is no significant influence of urban aerosols on the retrievals of dust-related conversion factor in Wuhan. This dust-case data-set screening scheme may potentially be extended to the other polluted city sites more influenced by mixed dust. In the future, we expect to validate the obtained conversion factors by comparing with unmanned aerial vehicles (UAVs) in situ measurements (Marinou et al., 2019).

A case study on the dust-related heterogeneous nucleation process was presented. Applying the conversion factors obtained herein together with the parameterization scheme D10 and D15, the height profile of immersion-mode INPC and dust mass concentration before the presence of an ice-containing cloud was shown. The maximum dust mass concentration at an altitude of 8.1 km is only 2.6 µg m^{-3}; the corresponding INPC here is derived at 62.3 L^{-1} (D15) and was seemed to trigger the subsequent heterogeneous ice formation.

In the future, the conversion parameters obtained in this study will be used to study the seasonal and long-term variation of INPC vertical distributions over Wuhan (Tobo et al., 2020). We will also need to separate other different aerosol components and retrieve their corresponding POLIPHON conversion factors (Mamouri and Ansmann, 2017; Córdoba-Jabonero et al., 2018). Furthermore, the observations with millimeter-wave radar can give the ice crystal number concentration information within the cloud so that may realize the possible closure study of heterogeneous ice nucleation process (Ansmann et al., 2019a). Additionally, the retrieved dust mass concentration profiles can be used to verify the results from dust models such as NMME-DREAM (Konsta et al., 2021).

Data availability

Sun photometer and ground-based polarization lidar data used to generate the results of this paper are available at the website (doi:10.5281/zenodo.4683015). CALIPSO data used in this work can be accessed through the website https://subset.larc.nasa.gov. Wuhan radiosonde data can be obtained at the website http://weather.uwyo.edu/upperair/sounding.html. MODIS land cover type data product is available at the website https://ladsweb.modaps.eosdis.nasa.gov. HYSPLIT model can be run through the website https://ready.arl.noaa.gov/HYSPLIT_traj.php.

Author Contributions

Yun He conceived the research, analyzed the data, acquired the research funding, and wrote the manuscript. Yunfei Zhang analyzed the sun photometer data. Fuchao Liu reviewed and proofread the manuscript. Zhenping Yin and Yang Yi participated in the scientific discussions, reviewed and proofread the manuscript. Yifan Zhan spent efforts in running the GRASP-AOD algorithm. Fan Yi acquired the research funding and led the study.

Competing interests

The authors declare that they have no conflict of interest.

Acknowledgments

This work is supported by the National Natural Science Foundation of China [grant numbers 41927804, 42005101]; the Hubei Provincial Natural Science Foundation of China [grant number 2020CFB229]; the Fundamental Research Funds for the Central Universities [grant number 2042020kf0018]; and the Meridian Space Weather Monitoring Project (China). The authors thank the University of Wyoming for providing the Wuhan radiosonde data, the Atmospheric Science Data Central (ASDC) at the NASA Langley Research Center for providing the CALIPSO data, the Level 1 and Atmosphere Archive and Distribution System (LAADS) Distributed Active Archive Center (DAAC) at the NASA Goddard Space Flight Center for providing the MODIS land cover type data product, and the NOAA Air Resources Laboratory (ARL) for the HYSPLIT model. The authors also would like to acknowledge the use of GRASP inversion algorithm software (http://www.grasp-open.com) in this work. Finally, we thank the colleagues who participated in the operation of the lidar system at our site.

References

Ansmann, A., Petzold, A., Kandler, K., Tegen, I., Wendisch, M., Müller, D., Weinzierl, B., Müller, T., and Heintzenberg, J.: Saharan mineral dust experiments SAMUM-1 and SAMUM-2: What have we learned? Tellus B, 63, 403-429. doi:10.1111/j.1600-0889.2011.00555.x, 2011.

Ansmann, A., Seifert, P., Tesche, M., and Wandinger, U.: Profiling of fine and coarse particle mass: case studies of Saharan dust and Eyjafjallajökull/Grimsvötn volcanic plumes, Atmos. Chem. Phys., 12, 9399-9415. doi.org/10.5194/acp-12-9399-2012, 2012.

Ansmann, A., Mamouri, R.-E., Bühl, J., Seifert, P., Engelmann, R., Hofer, J., Nisantzi, A., Atkinson, J. D., Kanji, Z. A., Sierau, B., Vrekoussis, M., and Sciare, J.: Ice-nucleating particle versus ice crystal number concentration in altocumulus and cirrus embedded in Saharan dust: A closure study, Atmos. Chem. Phys., 19, 15087-15115. doi.org/10.5194/acp-19-15087-2019, 2019a.

Ansmann, A., Mamouri, R.-E., Hofer, J., Baars, H., Althausen, D., and Abdullaev, S. F.: Dust mass, cloud condensation nuclei, and ice-nucleating particle profiling with polarization lidar: updated POLIPHON conversion factors from global AERONET analysis, Atmos. Meas. Tech., 12, 4849-4865. doi.org/10.5149/amt-12-4849-2019, 2019b.

440 Ansmann, A., Ohneiser, K., Mamouri, R.-E., Knopf, D., Veselovskii, I., Baars, H., Engelmann, R. Foth, A., Jimenez, C., Seifert, P., and Barja, B.: Tropospheric and stratospheric wildfire smoke profiling with lidar: mass, surface area, CCN and INP retrieval, Atmos. Chem. Phys., doi.org/10.5194/acp-21-9779-2021, 2021.

Behrendt, A., and Nakamura, T.: Calculation of the calibration constant of polarization lidar and its dependency on atmospheric temperature, Opt. Express, 10(16), 805-817. doi.org/10.1364/OE.10.000805, 2002.

445 Benavent-Oltra, J., Román, R., Granados-Muñoz, M., Pérez-Ramírez, D., Ortiz-Amezcua, P., Denjean, C., Lopatin, A., Lyamani, H., Torres, B., Guerrero-Rascado, J., Fuertes, D., Dubovik, O., Chaikovsky, A., Olmo, F., Mallet, M., and Alados-Arboledas, L.: Comparative assessment of GRASP algorithm for a dust event over Granada (Spain) during ChArMEx-ADRIMED 2013 campaign, Atmos. Meas. Tech., 10, 4439-4457. doi.org/10.5194/amt-10-4439-2017, 2017.

Benavent-Oltra, J., Román, R., Casquero-Vera, J., Pérez-Ramírez, D., Lyamani, H., Ortiz-Amezcua, P., Bedoya-Velásquez, 450 A., de Arruda Moreira, G., Barreto, Á., Lopatin, A., Fuertes, D., Herrera, M., Torres, B., Dubovik, O., Guerrero-Rascado, J., Goloub, P., Olmo-Reyes, F., and Alados-Arboledas, L.: Different strategies to retrieve aerosol properties at night-time with the GRASP algorithm, Atmos. Chem. Phys., 19, 14149-14171. doi.org/10.5194/acp-19-14149-2019, 2019.

Cantrell, W. and Heymsfield, A.: Production of ice in tropospheric clouds, B. Am. Meteorol. Soc., 86, 795-807. 455 doi.org/10.1175/BAMS-86-6-795, 2005.

Chen, J., Wu, Z., Augustin-Bauditz, S., Grawe, S., Hartmann, M., Pei, X., Liu, Z., Ji, D., and Wex, H.: Ice-nucleating particle concentrations unaffected by urban air pollution in Beijing, China, Atmos. Chem. Phys., 18, 3523-3539. doi.org/10.5194/acp-18-3523-2018, 2018.

Chen, J., Wu, Z., Chen, J., Reicher, N., Fang, X., Rudich, Y., and Hu, M.: Size-resolved atmospheric ice-nucleating particles 460 during East Asian dust events, Atmos. Chem. Phys., 21, 3491-3506. doi.org/10.5194/acp-21-3491-2021, 2021.

Córdoba-Jabonero, C., Sicard, M., Ansmann, A., del Águila, A., and Baars, H.: Separation of the optical and mass features of particle components in different aerosol mixtures by using POLIPHON retrievals in synergy with continuous polarized Micro-Pulse Lidar (P-MPL) measurements, Atmos. Meas. Tech., 11, 4775-4795. doi.org/10.5194/amt-11-4775-2018, 2018.

465 DeMott, P., Prenni, A., Liu, X., Kreidenweis, S., Petters, M., Twohy, C., Richardson, M., Eidhammer, T., and Rogers, D.: Predicting global atmospheric ice nuclei distributions and their impacts on climate, P. Natl. Acad. Sci. USA, 107, 11217-11222. doi.org/10.1073/pnas.0910818107, 2010.

DeMott, P., Prenni, A., McMeeking, G., Sullivan, R., Petters, M., Tobo, Y., Niemand, M., Möhler, O., Snider, J., Wang, Z., and Kreidenweis, S.: Integrating laboratory and field data to quantify the immersion freezing ice nucleation activity of 470 mineral dust particles, Atmos. Chem. Phys., 15, 393-409. doi.org/10.5194/acp-15-393-2015, 2015.

Draxler, R., and Rolph, G.: HYSPLIT (Hybrid Single-Particle Lagrangian Integrated Trajectory) Model, Air Resources Laboratory, NOAA, Silver Spring, Md, USA, 2003. http://www.arl.noaa.gov/ready/hysplit4.html. (last access: 7 July 2021)

Dubovik, O., Holben, B., Eck, T., Smirnov, A., Kaufman, Y., King, M., Tanré and Slutsker, I.: Variability of absorption and optical properties of key aerosol types observed in worldwide locations, J. Atmos. Sci., 59(3), 590-608. doi.org/10.1175/1520-0469(2002)059<0590:VOAAOP>2.0.CO;2, 2002.

Dubovik, O., Lapyonok, T., Litvinov, P., Herman, M., Fuertes, D., Ducos, F., Lopatin, A., Chaikovsky, A., Torres, B., Derimian, Y., Huang, X., Aspetsberger, M., and Federspiel, C.: GRASP: A versatile algorithm for characterizing the atmosphere, *SPIE Newsroom*. doi.org/10.1117/2.1201408.005558, 2014.

Fernald, F. G.: Analysis of atmospheric lidar observations: some comments, Appl. Optics, 23, 652-653. doi.org/10.1364/AO.23.000652, 1984.

Field, P. R., Lawson, R. P., Brown, P. R. A., Lloyd, G., Westbrook, C., Moisseev, D., Miltenberger, A., Nenes, A., Blyth, A., Choularton, T., Connolly, P., Buehl, J., Crosier, J., Cui, Z., Dearden, C., DeMott, P., Flossmann, A., Heymsfield, A., Huang, Y., Kalesse, H., Kanji, Z. A., Korolev, A., Kirchgaessner, A., Lasher-Trapp, S., Leisner, T., McFarquhar, G., Phillips, V., Stith, J., & Sullivan, S.: Secondary Ice Production: Current State of the Science and Recommendations for the Future, Meteorol. Mon., 58, 7.1-7.20, doi.org/10.1175/AMSMONOGRAPHS-D-16-0014.1, 2017.

Freudenthaler, V., Esselborn, M., Wiegner, M., Heese, B., Tesche, M., Ansmann, A., Müller, D., Althausen, D., Wirth, M., Fix, A., Ehret, G., Knippertz, P., Toledano, C., Gasteiger, J., Garhammer, M., and Seefeldner, M.: Depolarization ratio profiling at several wavelengths in pure Saharan dust during SAMUM2006, Tellus B, 61(1), 165-179. doi.org/10.1111/j.1600-0889.2008.00396.x, 2009.

Friedl, Mark, Damien Sulla-Menashe - Boston University and MODAPS SIPS - NASA.: MCD12C1 MODIS/Terra+Aqua Land Cover Type Yearly L3 Global 0.05Deg CMG. NASA LP DAAC. doi.org/10.5067/MODIS/MCD12C1.006, 2015.

Hallett, J., and Mossop, S.: Production of secondary ice particles during the riming process, Nature, 249, 26-28. doi.org/10.1038/249026a0, 1974.

He, Y., and Yi, F.: Dust aerosols detected using a ground-based polarization lidar and CALIPSO over Wuhan (30.5N, 114.4E), China, Adv. Meteorol., Article ID 536762. doi.org/10.1155/2015/536762, 2015.

He, Y., Yi, F., Yi, Y., Liu, F., and Zhang, Y.: Heterogeneous nucleation of midlevel cloud layer influenced by transported Asian dust over Wuhan (30.5°N, 114.4°E), China, J. Geophys. Res.-Atmos., 126(2), e2020JD033394. doi.org/10.1029/2020JD033394, 2021a.

He, Y., Liu, F., Yin, Z., Zhang, Y., Zhan, Y., and Yi, F.: Horizontally Oriented ice crystals observed by the synergy of zenith- and slant-pointed polarization lidar over Wuhan (30.5°N, 114.4°E), China, J. Quant. Spectrosc. Radiat. Transf., 268, 107626. doi.org/10.1016/j.jqsrt.2021.107626, 2021b.

Hofer, J., Ansmann, A., Althausen, D., Engelmann, R., Baars, H., Abdullaev, S., and Makhmudov, A.: Long-term profiling of aerosol light extinction, particle mass, cloud condensation nuclei, and ice-nucleating particle concentration over Dushanbe, Tajikistan, in Central Asia, Atmos. Chem. Phys.*,* 20, 4695-4711. doi.org/10.5194/acp-20-4695-2020, 2020.

505 Holben, B., Eck, T., Slutsker, I., Tanré, D., Buis, J., Setzer, A., Vermote, E., Reagan, J., Kaufman, Y., Nakajima, T., Lavenu, F., Jankowiak, I., and Smirnov, A.: AERONET—A federated instrument network and data archive for aerosol characterization, Remote Sens. Environ. 66(1), 1-16. doi.org/10.1016/s0034-4257(98)00031-5, 1998.

Hoose, C., Kristjánsson, J., Chen, J.-P., and Hazra, A.: A classical-theory-based parameterization of heterogeneous ice nucleation by mineral dust, soot, and biological particles in a global climate model, J. Atmos. Sci., 67(8), 2483-2503.

510 doi.org/10.1175/2010JAS3425.1, 2010.

Hu, Q., Wang, H., Goloub, P., Li, Z., Veselovskii, I., Podvin, T., Li, K., and Korenskiy, M.: The characterization of Taklamakan dust properties using a multiwavelength Raman polarization lidar in Kashi, China, Atmos. Chem. Phys., 20, 13817-13834. doi.org/10.5194/acp-20-13817-2020, 2020.

Huang, J., Minnis, P., Chen, B., Huang, Z., Liu, Z., Zhao, Q., Yi, Y., and Ayers, J.; Long-range transport and vertical struc-

515 ture of Asian dust from CALIPSO and surface measurements during PACDEX, J. Geophys. Res.-Atmos., 113, 23, D23212. doi.org/10.1029/2008JD010620, 2008.

IPCC. 2013: Climate change: The physical science basis. In Contribution of Working Group I to the Fifth Assessment Report of the Intergovernmental Panel on Climate Change, Cambridge University Press. doi.org/10.1016/S0925-7721(01)00003-7.

520 Jiang, H., Yin, Y., Wang, X., Gao, R., Yuan, L., Chen, K., and Shan, Y.: The measurement and parameterization of ice nucleating particles in different backgrounds of China, Atmos. Res., 181, 72-80. dx.doi.org/10.1016/j.atmosres.2016.06.013, 2016.

Kanji, Z. A., Ladino, L. A., Wex, H., Boose, Y., Burkert-Kohn, M., Cziczo, D. J., and Krämer, M.: Overview of ice nucleating particles, Meteorol. Mon., 58, 1.1-1.33. doi.org/10.1175/AMSMONOGRAPHS-D-16-0006.1, 2017.

525 Kanji, Z. A., Welti, A., Corbin, J. C., and Mensah, A. A.: Black carbon particles do not matter for immersion mode ice nucleation, Geophys. Res. Lett., 46, e2019GL086764, doi.org/10.1029/2019GL086764, 2020.

Kojima, T., Buseck, P., Iwasaka, Y., Matsuki, A., and Trochkine, D.: Sulfate-coated dust particles in the free troposphere over Japan, Atmos. Res., 82, 3-4, 698-708, doi.org/10.1016/j.atmosres.2006.02.024, 2006.

Kong, W., and Yi, F.: Convective border layer evolution from lidar backscatter and its relationship with surface aerosol con-

530 centration at a location of a central China megacity, J. Geophys. Res.-Atmos., 120, 7928-7940. doi.org/10.1002/2015JD023248, 2015.

Konsta, D., Tsekeri, A., Solomos, S., Siomos, N., Gialitaki, A., Tetoni, E., Lopatin, A., Goloub, P., Dubovik, O., Amiridis, V., and Nastos, P.: The potential of GRASP/GARRLiC retrievals for dust aerosol model evaluation: case study during the PreTECT Campaign, Remote Sens., 13(5), 873. doi.org/10.3390/rs13050873, 2021.

535 Liu, F., Yi, F., Yin, Z., Zhang Y., He, Y., and Yi, Y.: Measurement report: characteristics of clear-day convective boundary layer and associated entrainment zone as observed by a ground-based polarization lidar over Wuhan (30.5°N, 114.4° E), Atmos. Chem. Phys., 21, 2981-2998. doi.org/10.5194/acp-21-2981-2021, 2021.

Ma, Y., Zhang, M., Jin, S., Gong, W., Chen, N., Chen, Z., Jin, Y., and Shi, Y.: Long-term investigation of aerosol optical and radiative characteristics in a typical megacity of central China during winter haze periods, J. Geophys. Res.-Atmos., 124, 12093-12106. doi.org/10.1029/2019JD030840, 2019.

Mamali, D., Marinou, E., Sciare, J., Pikridas, M., Kokkalis, P., Kottas, M., Binietoglou, I., Tsekeri, A., Keleshis, C., Engelmann, R., Baars, H., Ansmann, A., Amiridis, V., Russchenberg, H., and Biskos, G.: Vertical profiles of aerosol mass concentration derived by unmanned airborne in situ and remote sensing instruments during dust events, Atmos. Meas. Tech., 11, 2897-2910. doi.org/10.5194/amt-11-2897-2018, 2018.

Mamouri, R. E., Ansmann, A., Nisantzi, A., Kokkalis, P., Schwarz, A., and Hadjimitsis, D.: Low Arabian extinction-to-backscatter ratio, Geophys. Res. Lett., 40, 4762–4766. doi.org/10.1002/grl.50898, 2013.

Mamouri, R. E. and Ansmann, A.: Fine and Coarse dust separation with polarization lidar, Atmos. Meas. Tech., 7, 3717-3735. doi.org/10.5194/amt-7-3717-2014, 2014.

Mamouri, R. E. and Ansmann, A.: Estimated desert-dust ice nuclei profiles from polarization lidar: methodology and case studies, Atmos. Chem. Phys., 15, 3463-3477. doi.org/10.5194/acp-15-3463-2015, 2015.

Mamouri, R. E. and Ansmann, A.: Potential of polarization lidar to provide profiles of CCN- and INP-relevant aerosol parameters, Atmos. Chem. Phys., 16, 5905-5931. doi.org/10.5194/acp-16-5905-2016, 2016.

Mamouri, R. E. and Ansmann, A.: Potential of polarization/Raman lidar to separate fine dust, coarse dust, maritime, and anthropogenic aerosol profiles, Atmos. Meas. Tech., 10, 3403-3427. doi.org/10.5194/amt-10-3403-2017, 2017.

Marinou, E., Tesche, M., Nenes, A., Ansmann, A., Schrod, J., Mamali, D., Tsekeri, A., Pikridas, M., Baars, H., Engelmann, R., Voudouri, K.-A., Solomos, S., Sciare, J., Groß, S., Ewald, F., and Amiridis, V.: Retrieval of ice-nucleating particle concentrations from lidar observations and comparison with UAV in situ measurements, Atmos. Chem. Phys., 19, 11315-11342. doi.org/10.5194/acp-19-11315-2019, 2019.

Murray, B. J., O'Sullivan, D., Atkinson, J. D., and Webb, M. E.: Ice nucleation by particles immersed in supercooled cloud droplet, Chem. Soc. Rev., 41, 6519-6554. doi.org/10.1039/c2cs35200a, 2012.

Mülmenstädt, J., Sourdeval, O., Delanoë, J., and Quaas, J.: Frequency of occurrence of rain from liquid-, mixed-, and ice-phase clouds derived from A-Train satellite retrievals, Geophys. Res. Lett., 42, 6502-6509. doi.org/10.1002/2015GL06460, 2015.

Nash, J., Oakley, T., Vömel, H., and Li, W.: WMO Intercomparison of high quality radiosonde systems, Yangjiang, China, 12 July – 2 August 2010, World Meteorological Organization Instruments and Observing methods, Report IOM-107, WMO/TD No. 1580, 2011. https://www.wmo.int/pages/prog/www/IMOP/publications-IOM-series.html. (last access: 7 July 2021)

Omar, A. H., Winker, D. M., Kittaka, C., Vaughan, M. A., Liu, Z., Hu, Y., Rogers, R. R., Ferrare, R. A., Lee, K.-P., Kuehn, R. E., and Hostetler, C. A.: The CALIPSO Automated Aerosol Classification and Lidar Ratio Selection Algorithm, J. Atmos. Ocean Tech., 26(10), 1994-2014. doi.org/10.1175/2009JTECHA1231.1, 2009.

O'Neill, N., Dubovik, O., and Eck, T. F.: A modified Ångström coefficient for the characterization of sub-micron aerosols, Appl. Optics, 40(14), 2368-2375. doi.org/10.1364/AO.40.002368, 2001.

O'Neill, N., Eck, T., Smirnov, A., Holben, B., and Thulasiraman, S.: Spectral discrimination of coarse and fine mode optical depth, J. Geophys. Res., 108(D17), 4559. doi.org/10.1029/2002jd002975, 2003.

575 Peng, L., Yi, F., Liu, F., Yin, Z. and He, Y.: Optical properties of aerosol and cloud particles measured by a single-line-extracted pure rotational Raman lidar, Opt. Express, 29(14), 21947-21964. doi.org/10.1364/OE.427864, 2021.

Rosenfeld, D., Lohmann, U., Raga, G. B., O'Dowd, C. D., Kulmala, M., Fuzzi, S., Reissell, A., and Andreae, M. O.: Flood or drought: How do aerosols affect precipitation? Science, 321, 1309-1313. doi:10.1126/science.1160606, 2008.

Rosenfeld, D., Andreae, M. O., Asmi, A., Chin, M., Leeuw, G., Donovan, D. P., Kahn, R., Kinne, S., Kivekäs, N., Kulmala, 580 M., Lau, W., Schmidt, K. S., Suni, T., Wagner, T., Wild, M., and Quaas, J.: Global observations of aerosol-cloud-precipitation-climate interactions, Rev. Geophys., 52, 750-808. doi.org/10.1002/2013RG000441, 2014.

Sakai, T., Nagai, T., Zaizen, Y., and Mano, Y.: Backscattering linear depolarization ratio measurements of mineral, sea-salt, and ammonium sulfate particles simulated in a laboratory chamber. Appl. Optics, 49, 4441-4449. doi.org/10.1364/AO.49.004441, 2010.

585 Schill, G. P., DeMott, P. J., Emerson, E., W. Rauker, A. M. C., Kodros, J. K., Suski, K. J., Hill, T., C. J., Levin, E. J. T., Pierce, J. R., Farmer, D. K., and Kreidenweis, S. M.: The contribution of black carbon to global ice nucleating particle concentrations relevant to mixed-phase clouds, P. Natl. Acad. Sci. USA, 117(37), 22705-22711, doi.org/ 10.1073/pnas.2001674117, 2020.

Shao, J., Yi, F., and Yin, Z.: Aerosol layers in the free troposphere and their seasonal variations as observed in Wuhan, Chi-590 na, Atmos. Environ., 224, 117323. doi.org/10.1016/j.atmosenv.2020.117323, 2020.

Tesche, M., Ansmann, A., Müller, D., Althausen, D., Engelmann, R., Freudenthaler, V., and Groß, S.: Vertically resolved separation of dust and smoke over Cape Verde using multiwavelength Raman and polarization lidars during Saharan Mineral Dust Experiment 2008, J. Geophys. Res., 114, D13202. doi.org/10.1029/2009JD011862, 2009.

Tobo, Y., Uetake, J., Matsui, H., Moteki, N., Uji, Y., Iwamoto, Y., Miura, K., and Misumi, R.: Seasonal trends of atmos-595 pheric ice nucleating particles over Tokyo, J. Geophys. Res.-Atmos., 125, e2020JD033658. doi.org/10.1029/2020JD033658, 2020.

Torres, B., Dubovik, O., Fuertes, D., Schuster, G., Cachorro, V. E., Lapyonok, T., Goloub, P., Blarel, L., Barreto, A., Mallet, M., Toledano, C., and Tanré, D.: Advanced characterisation of aerosol size properties from measurements of spectral optical depth using the GRASP algorithm, Atmos. Meas. Tech., 10, 3743-3781. doi.org/10.5194/amt-10-3743-2017, 600 2017.

Torres, B. and Fuertes, D.: Characterization of aerosol size properties from measurements of spectral optical depth: a global validation of the GRASP-AOD code using long-term AERONET data, Atmos. Meas. Tech., 14, 4471-4506, doi.org/10.5194/amt-14-4471-2021, 2021.

Ullrich, R., Hoose, C., Möhler, O., Niemand, M., Wagner, R., Höhler, K., Hiranuma, N., Saathoff, H., and Leisner, T.: A
605   new ice nucleation active site parameterization for desert dust and soot, J. Atmos. Sci., 74, 699-717.
doi.org/10.1175/JASD-16-0074.1, 2017.

Wagner, F., Bortoli, D., Pereira, S., Costa, M. J., Silva, A. M., Weinzierl, B., Esselborn, M., Petzold, A., Rasp, K., Heinold
B., and Tegen, I.: Properties of dust aerosol particles transported to Portugal from the Sahara desert, Tellus B: Chem.
Phys. Meteorol., 61(1), 297-306. doi.org/10.1111/j.1600-0889.2008.00393.x, 2009.

610   Wang, T., Han, Y., Hua, W., Tang, J., Huang, J., Zhou, T., Huang, Z., Bi, J., and Xie, H.: Profiling dust mass concentration
in Northwest China using a joint lidar and sun-photometer setting, Remote Sens., 13, 1099. doi.org/10.3390/rs13061099,
2021.

Winker, D., Hunt, W., and McGill, M.: Initial performance assessment of CALIOP, Geophys. Res. Lett., 34(19), L19803.
doi.org/10.1029/2007GL030135, 2007.

615   Yin, Z., Yi, F., He, Y., Liu, F., Yu, C., and Zhang, Y.: Asian dust impacts on heterogeneous ice formation at Wuhan based
on polarization lidar measurements, Atmos. Environ., 246(11), 118166. doi.org/10.1016/j.atmosenv.2020.118166,
2021a.

Yin, Z., Yi, F., Liu, F., He, Y., Zhang, Y., Yu, C., and Zhang, Y.: Long-term variations of aerosol optical properties over
Wuhan with polarization lidar, Atmos. Environ., 259, 118508, doi.org/10.1016/j.atmosenv.2021.118508, 2021b.

620   Zhang, Y., Yi, F., Kong, W., and Yi, Y.: Slope characterization in combining analog and photon count data from atmospher-
ic lidar measurements, Appl. Optics, 53(31), 7312-7320. doi.org/10.1364/AO.53.007312, 2014.

Zhang, Y., Yu, F., Luo, G., Chen, J.-P., and Chou, C.: Impact of mineral dust on summertime precipitation over the Taiwan
region, J. Geophys. Res.-Atmos., 125, e2020JD033120. doi.org/10.1029/2020JD033120, 2020.

Zhang, Y., Zhang, Y., Yu, C., and Yi, F.: Evolution of aerosols in the atmospheric boundary layer and elevated layers during
625   a severe, persistent haze episode in a central China megacity, Atmosphere, 12, 152. doi.org/10.3390/atmos12020152,
2021.
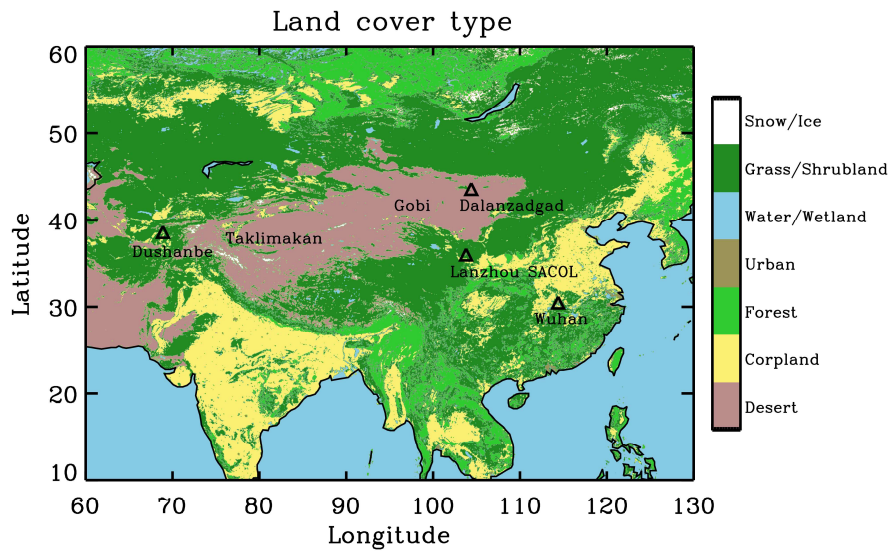
630

Figure 1: The land cover type during January 2019 – February 2020 over Eastern Asia region (60-130°E, 10-60°N) obtained from the MODIS (combined Aqua and Terra) Collection 6 level-3 MCD12C1 product (with 0.05° resolution). The locations of three AERONET sites Dushanbe (38.6°N, 68.8°E), Dalanzadgad (43.6°N, 104.4°E), and Lanzhou SACOL (36.0°N, 104.1°E) as well as the central China city Wuhan (30.5°N, 114.4°E) are marked with the hollow black triangles. The general locations of the Gobi Desert

635 **and Taklimakan Desert are also marked as seen in the brown areas (Friedl et al., 2015).**
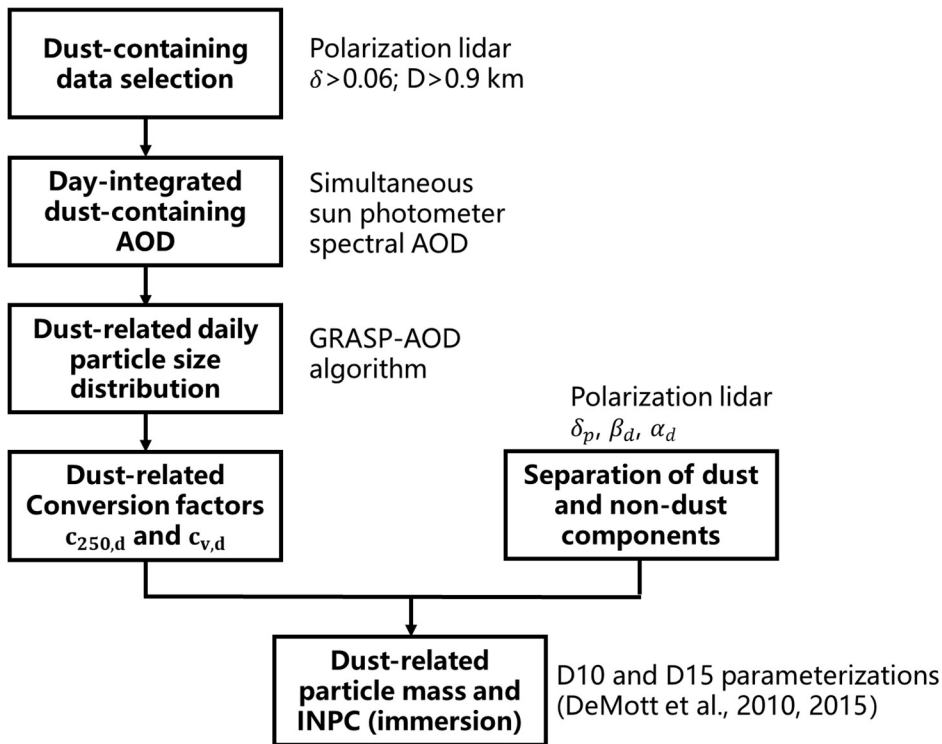
Figure 2: Overview of the data analysis scheme in this work. The left column shows the specific steps for retrieving the dust-related conversion factors over Wuhan. GRASP-AOD algorithm is used as an auxiliary for deriving the particle size distribution from sun-photometer-measured spectral AODs.
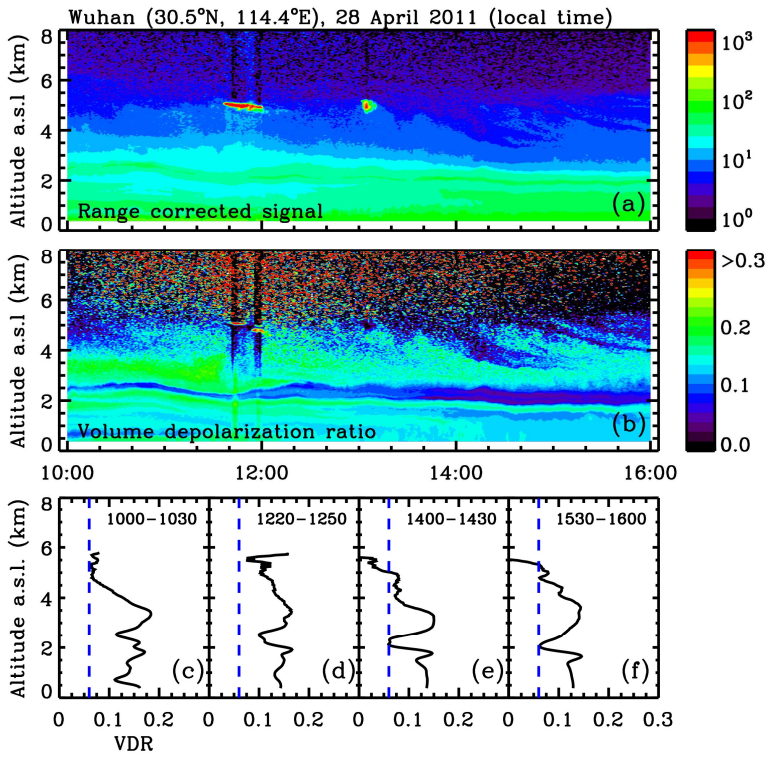
Figure 3: Time-height contour plots (1 minute/30 m resolution) of (a) range-corrected signal and (b) volume depolarization ratio and 30-minute integrated profiles of volume depolarization ratio during (c) 1000-1030LT, (d) 1220-1250LT, (e) 1400-1430LT, and (f) 1530-1600LT measured by a 532 nm polarization lidar on 28 April 2011. The vertical dashed blue lines indicate the volume depolarization ratio value of 0.06 that is considered as a threshold for the identification of dust occurrence.
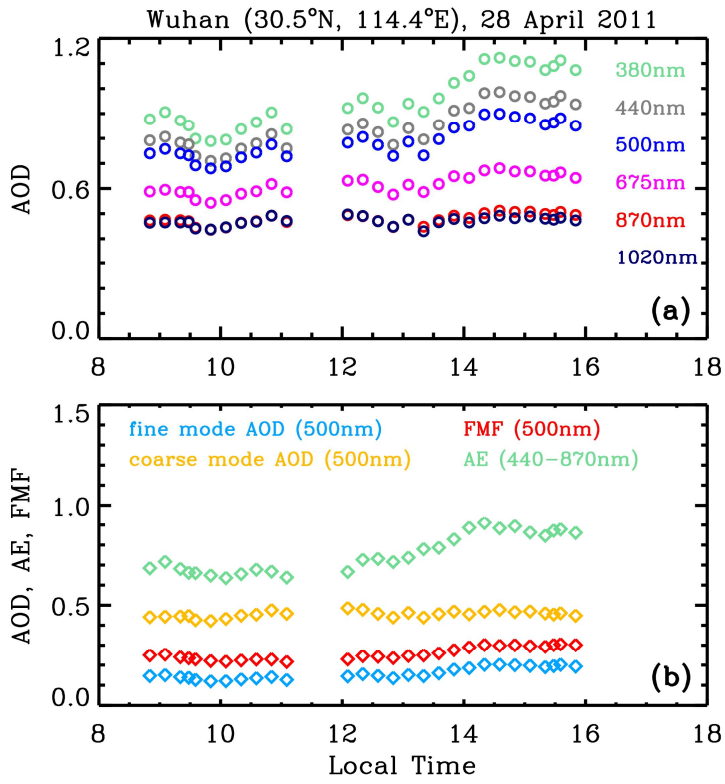
650 **Figure 4: Time series of (a) AOD at six wavelengths (380 nm, 440 nm, 500 nm, 675 nm, 870 nm, 1020 nm) and (b) 500 nm fine mode AOD (azure rhombi), coarse mode AOD (yellow rhombi), fine-mode AOD fraction (FMF, red rhombi), and Ångström exponent for the 440-870 nm wavelength range (AE, aquamarine rhombi) observed with sun photometer at Wuhan (30.5°N, 114.4°E) on 28 April 2011.**
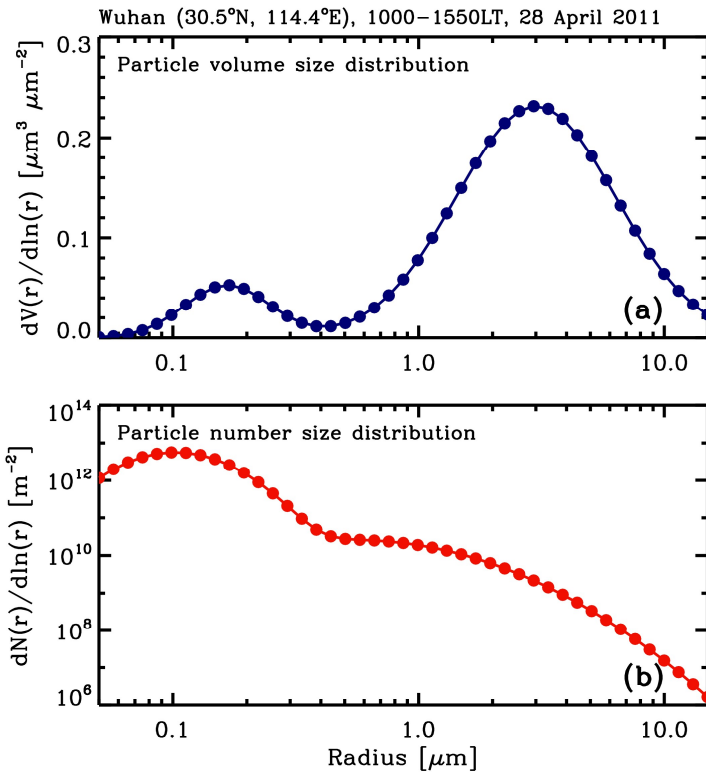
655

Figure 5: Column-integrated (a) particle volume size distribution and (b) particle number size distribution derived from sun photometer observations at Wuhan (30.5°N, 114.4°E) during 1000-1550 LT on 28 April 2011 based on GRASP-AOD algorithm. Ground-based polarization lidar observation verified that dust episodes occurred during this period.
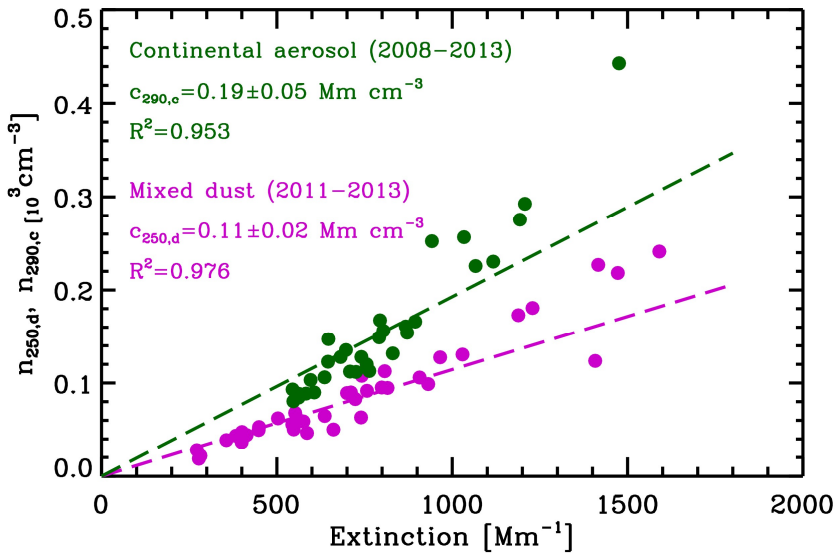
660

Figure 6: **Relationship between extinction coefficient and large particle (with radius >250 nm) number concentration $n_{250,d}$ for mixed dust and $n_{290,c}$ for continental aerosols over Wuhan. Each green point denotes a pair of daily averaged values for the dust-occurring period of a dust-intrusion day (verified by ground-based polarization lidar). Each purple point denotes a pair of daily averaged values during the period when Ångström exponent >1.6. The conversion factor $c_{250,d} = 0.19 \pm 0.05$ Mm cm^{-3} is obtained during 2011-2013 and $c_{290,c} = 0.11 \pm 0.02$ Mm cm^{-3} is obtained during 2008-2013 (see Equations (4) and (5) in Mamouri and Ansmann (2016)).**

665
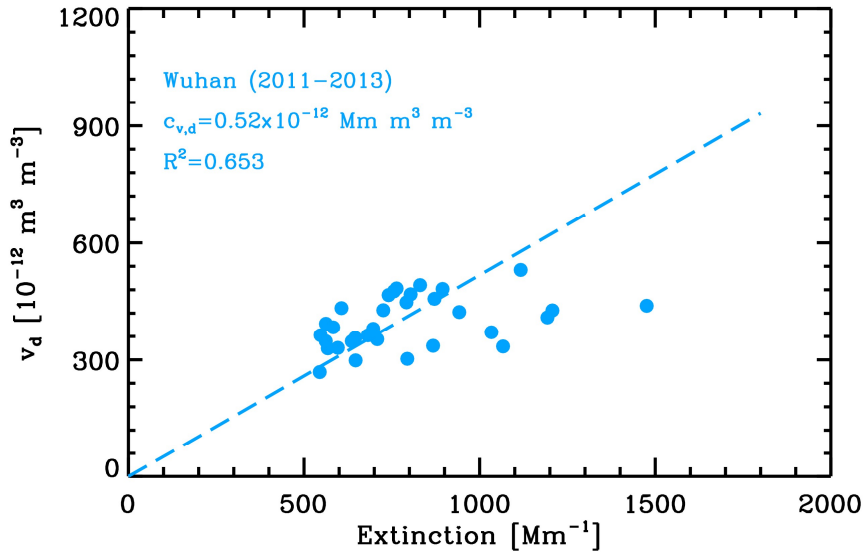
670 **Figure 7: Relationship between extinction coefficient and volume concentration v_d for mixed dust. Correlations are given by sun photometer observations during dust-intrusion days that are verified by ground-based polarization lidar. Each point denotes a pair of daily averaged values for the dust-occurred period of a dust-intrusion day. The slope of the black dashed line indicates the mean increase in v_d with extinction coefficient, which is defined as the extinction-to-volume conversion factor $c_{v,d} = (0.52 \pm 0.12) \times 10^{-12}$ Mm m^{3}m^{-3}. All the points are obtained from the dust-intrusion days during 2011-2013.**

675
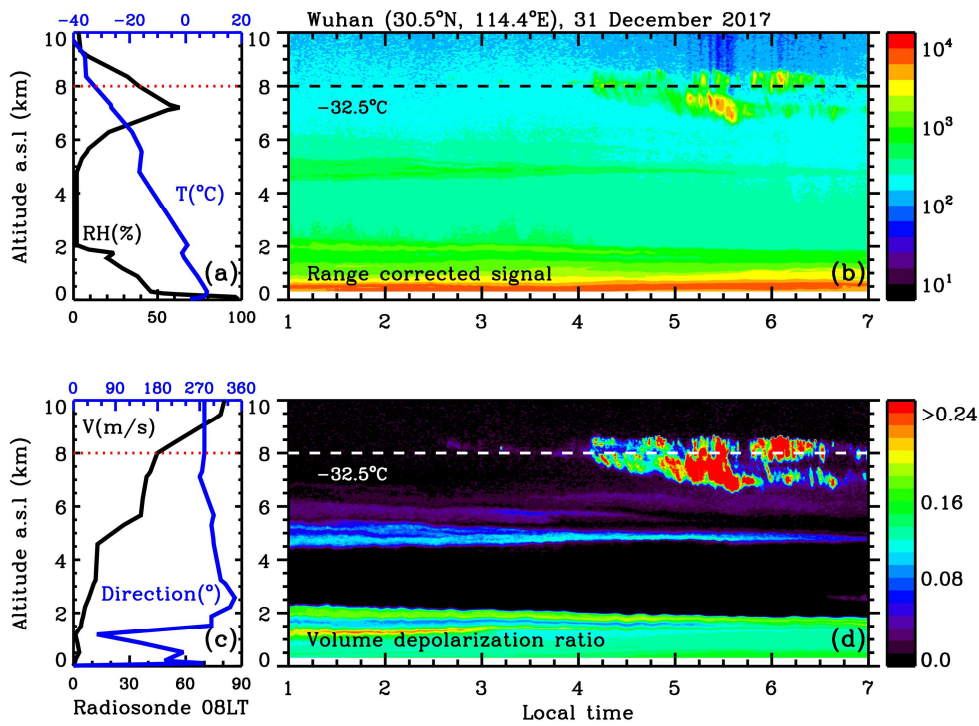
Figure 8: Time-height contour plots (1 minute/30 m resolution) of (b) range-corrected signal and (d) volume depolarization ratio measured by a 532 nm polarization lidar on 31 December 2017. Height profiles of (a) temperature and relative humidity, and (c) wind speed and wind direction measured with the radiosonde launched at 0800 LT. Horizontal lines indicate the -32.5°C temperature height levels.

680
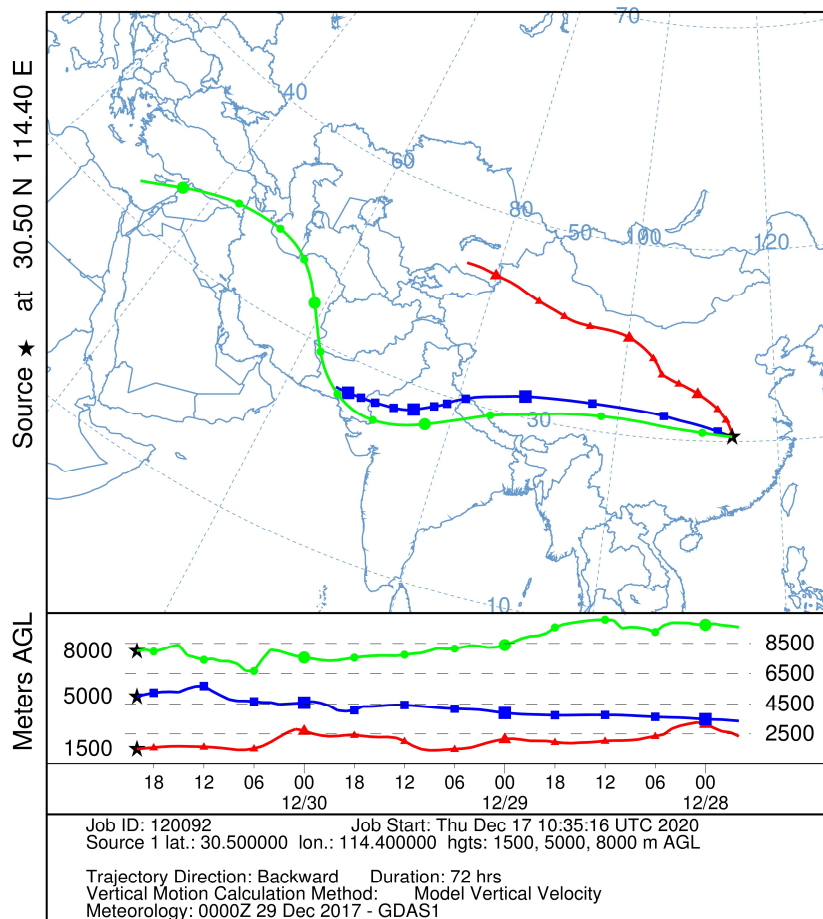
Figure 9: Three-day backward trajectories starting from Wuhan at 2000 UTC on 30 December 2017 (at 1.5 km, 5.0 km, and 8.0 km) are computed using the HYSPLIT model (Draxler and Rolph, 2003).

685
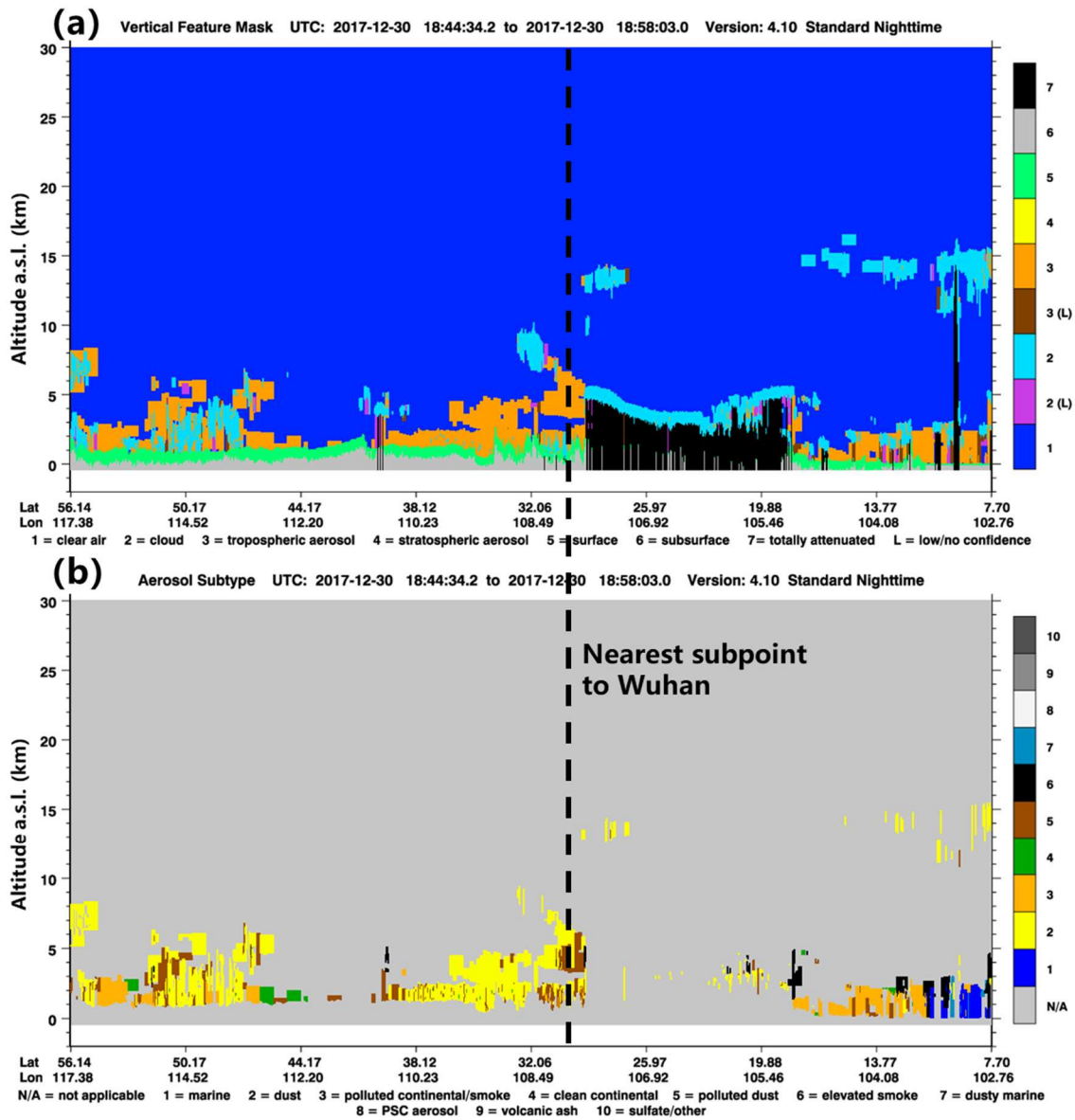
Figure 10: CALIPSO altitude-orbit cross-section measurements of level-2 (a) vertical feature mask and (b) aerosol subtype product from 18:44:34 UTC to 18:58:03 UTC on 30 December 2017. The corresponding orbit is 2017-12-30T18-31-05ZN. The vertical dashed line denotes the location of the nearest subpoint to Wuhan.

690
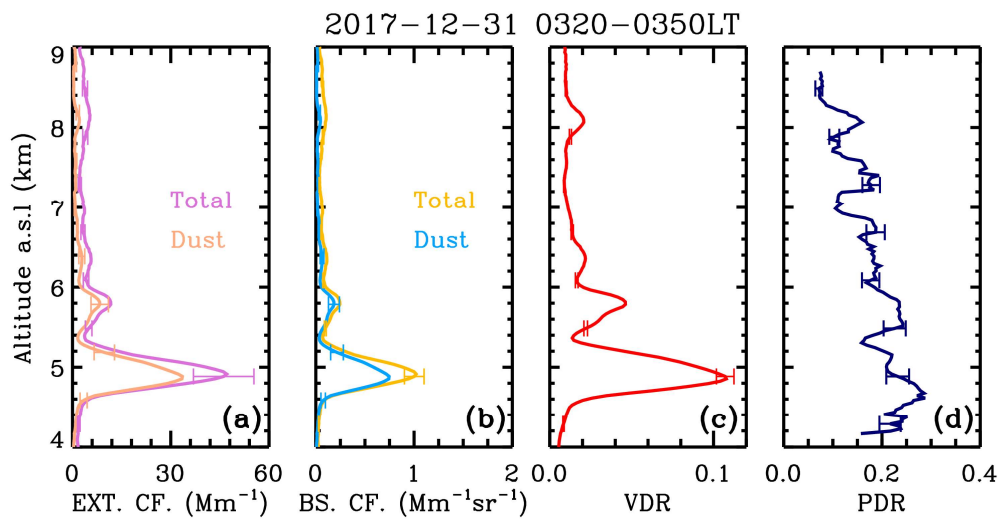
Figure 11: Profiles of the (a) dust and total (dust + non-dust) extinction coefficient, (b) dust and total (dust + non-dust) backscatter coefficient, (c) volume depolarization ratio δ, and (d) particle depolarization ratio δ_p derived by the 532 nm polarization lidar during 0320-0350 LT on 31 December 2017. Horizontal error bars denote the relative errors of each parameter.

695
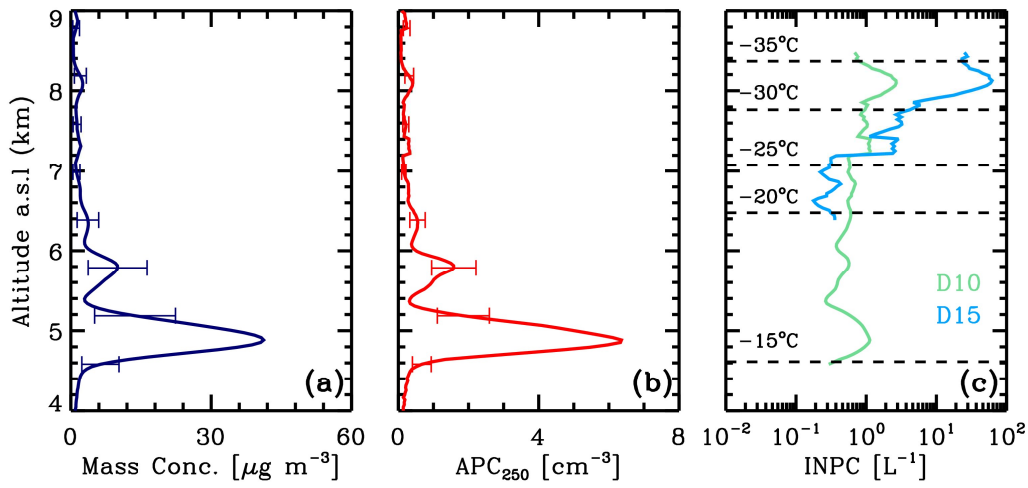
Figure 12: Profiles of the (a) dust mass concentration M_d, (b) particle number concentration APC$_{250}$, (c) ice-nucleating particle concentration derived by the POLIPHON method (D10 and D15 parameterizations) during 0320-0350 LT on 31 December 2017. Horizontal dashed lines denote the temperature height levels of -15 °C, -20 °C, -25 °C, -30 °C, and -35 °C.

700